Int. J. Electrochem. Sci., 17 **(2022)** Article Number: 221145, doi: 10.20964/2022.11.32

International Journal of
ELECTROCHEMICAL
SCIENCE
www.electrochemsci.org

Preparation of Porous Carbon from Buckwheat Husk and its Electrochemical Properties

Qi Zhang, Junlong Wang, Meigen Deng[*]

Key Laboratory of Electric Energy Storage & Conversion of Jiangxi Province, Jiangxi University of Finance & Economics, Nanchang 330013, Jiangxi, China
[*]E-mail: dengmeigen@jxufe.edu.cn

Received: 31 August 2022 / *Accepted:* 24 September 2022 / *Published:* 10 October 2022

To reduce environmental pollution and recycle biomass waste, high value-added activated carbon (AC) for supercapacitors was prepared from buckwheat husk with KOH as the activating agent. The relationship between the amount of KOH and the porosity of the ACs was studied. Thermogravimetric analysis (TG), X-ray diffraction (XRD), Raman, scanning electron microscopy (SEM) and N_2 adsorption were used to characterize the morphology and structure of the materials. Cyclic voltammetry (CV) and galvanostatic charge-discharge (GCD) were also employed to analyze the electrochemical performance of the electrodes and supercapacitors based on the ACs in 0.5 M Na_2SO_4. The results show that AC prepared with a KOH/char ratio of 5:1 possesses a high specific surface area of 2347 $m^2 g^{-1}$ and a suitable pore size distribution, with micropores distributed mainly in the range from 1 to 2 nm, mesopores between 2 to 4 nm, and an average pore diameter of 2.1 nm. A utilization rate of specific surface area up to 63% is obtained. At a current density of 1 A g^{-1}, a specific capacitance of 295 F g^{-1} is achieved. At a power density of 500 W kg^{-1}, the supercapacitor based on the prepared AC has a high energy density of 12.3 Wh kg^{-1}. Even if the power density is increased by a factor of 30, the energy density retention rate still reaches 70.5%. After 3000 charge-discharge cycles, the specific capacitance retention rate remains at 98.5%. This study developed a high value-added utilization approach for large amounts of buckwheat husks worldwide that are difficult to dispose of.

Keywords: biomass waste; buckwheat husk; porous carbon; supercapacitor

1. INTRODUCTION

As a new kind of energy storage device between batteries and traditional capacitors, supercapacitors are characterized by high power density, high energy density, long lifetime, wide operating temperature and freedom from maintenance. The supercapacitor has a wide range of applications in consumer electronics, communications, transportation, aerospace and other fields. The electrode materials of supercapacitors are focused mainly on porous carbon materials with high specific surface areas, metal oxides, conductive polymers and various composite materials [1-3]. Activated

carbon (AC) is the most commonly used electrode material for supercapacitors due to its wide range of raw material sources, mature production technology, stable structure, high power density and relatively low price. The electrode materials of various commercial supercapacitors are mainly porous AC with a high specific surface area. At present, the precursors of commercial ACs are mainly fossil fuels (coal and petroleum coke, etc.) and various woods, which not only consume valuable resources but are also high in preparation cost. Therefore, it is very urgent to find cheap and high-quality raw materials.

In recent years, under the dual requirements of environmental protection and waste utilization, the preparation of AC from biomass waste has become an important research hotspot in the field of energy storage [4]. The main work of biomass waste-based AC research is to optimize various biomass wastes, such as corn stalks [5], banana leaves [6], soybeans [7], grape marcs [8], orange peel [9], and kapok [10]. Another important area is the doping study of biomass waste AC, including doping with elements such as N, O, P, and S [11-15].

As an important raw food material, buckwheat is widely cultivated and has a large output. A large amount of buckwheat husk is produced in buckwheat processing worldwide every year. Due to the lack of suitable application paths, most buckwheat husk is burned, which not only wastes resources but also causes serious air pollution. In fact, buckwheat husk has a high density and high lignin and cellulose content, making it a high-quality AC precursor that is especially suitable for the preparation of AC for supercapacitors with high added value. At present, buckwheat husk was reported to have been used to prepare AC as an adsorbent material for purification purposes [16] and as a negative electrode material for lithium-ion batteries [17], but there are few reports on its use as an electrode material for supercapacitors. In this paper, high-quality AC for supercapacitors was developed using buckwheat husk as the precursor, and its porosity and electrochemical properties were investigated in detail.

2. EXPERIMENTATION

2.1 Experimental materials

The buckwheat husk used in the experiment comes from the rural area of Shanxi Province (China). HCl, KOH and Na_2SO_4 were of analytical grade and produced by Xilong Chemical Co., Ltd. (Guangzhou, China). Conductive carbon black (super Li) is from Timical, Switzerland. Polytetrafluoroethylene emulsion (D210C, 60% solid content) was purchased from Daikin, Japan. Except for buckwheat hull, all materials were used as received.

2.2 Preparation of AC

After being washed and fully dried, the buckwheat husk was poured into a stainless-steel crucible, placed in a furnace and carbonized at 500 °C for 2 h under a nitrogen atmosphere to obtain buckwheat husk-based char (BHC). Subsequently, KOH and BHC were fully mixed at a KOH/BHC mass ratio of x (x=2, 3, 4 and 5). The mixture was heated first at 500 °C for 1 h and then 800 °C for 2 h in a furnace under a N_2 atmosphere. After being cooled, the product was first boiled with dilute aqueous

HCl solution, then washed with deionized water until neutral, and finally dried at 110 °C for 24 h. The product is labeled AC-x, which represents activated carbon prepared at an alkali-char ratio of x.

2.3. Fabrication of supercapacitor

To fabricate electrodes, AC, conductive carbon black and polytetrafluoroethylene emulsion were mixed with mass proportions of 75%, 20% and 5%, respectively. After being dried to a certain extent, the mixture was evenly spread on the foamed nickel collectors and pressed into sheet electrodes with a diameter of 8 mm and a thickness of approximately 0.5 mm. For supercapacitor assembly, two electrodes with a piece of separator between were encapsulated into a steel case. The electrolyte was a 0.5 mol L^{-1} aqueous Na_2SO_4 solution.

2.4. Characterization of AC

Thermogravimetric (TG) measurements were carried out on a DSC-TG STA 409 (Netzsch, Germany) under a N_2 atmosphere in the range of 20~800 °C at a scan rate of 10 °C min^{-1}. X-ray diffraction (XRD) patterns were obtained from a Rigaku Smart Lab (9) diffractometer (Rigaku, Germany). The tested angle range is from 10 to 90 degrees. Raman measurements were conducted on a Thermo-DXR-2xi in the range of 500~3000 nm^{-1} with a laser wavelength of 532 nm. Scanning electron microscope (SEM) investigations were performed on a Hitachi SU8020. Using N_2 as an adsorbate, a Micromeritics ASAP2000 was employed to characterize the porosity of the samples. Before testing, all samples were degassed at 300 °C for 24 h. The specific surface area was calculated by the Brunauer-Emmett-Teller method and denoted S_{BET}. The t-plot method was deployed to calculate the specific surface area of micropores (S_{micro}) and volume of micropores (V_{micro}). By using the N_2 adsorption data and assuming a slit pore geometry, density function theory was used to obtain the pore size distribution (PSD) of the samples.

2.5. Electrochemical measurement

An IM6EX electrochemical workstation (Zahner, Germany) was used to characterize the cyclic voltammetry (CV) properties of all samples using a three-electrode configuration in a 0.5 mol L^{-1} aqueous Na_2SO_4 solution with scan rates from 2 to 20 mV s^{-1} and a voltage range of -0.4~0.8 V. The counter and reference electrode were Pt pellet and Ag/AgCl, respectively. A battery analyzer model (Landian, China) was deployed to perform the galvanostatic charge-discharge (GCD) test with a two-electrode configuration at various current densities. The specific gravimetric capacitance (C_g, F g^{-1}) was calculated from the discharge curve by applying Equation (1):

$$C_g = 2I\Delta t / (m\Delta V) \quad (1)$$

where I (A) is the discharge current, Δt (s) is the discharge time, m (g) is the average mass of a single electrode, and ΔV (V) is the voltage change during discharge [18]. The energy density (E, Wh kg^{-1}) and power density (P, W kg^{-1}) of the supercapacitors were calculated according to Equations (2-3):

$$E = C_g (\Delta V)^2 / (8 \times 3.6) \quad (2)$$

$$P = 3600E / \Delta t \quad (3)$$

where C_g (F g^{-1}) is the specific gravimetric capacitance, ΔV (V) is the cell voltage excluding the IR drop during the discharging process, and Δt (s) is the discharge time [19, 20].

3. RESULTS AND DISCUSSION

3.1 Morphology and structure

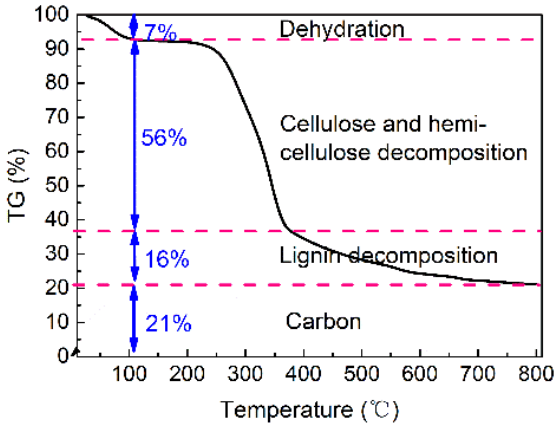

Figure 1. Thermogravimetric analysis of buckwheat husk

The buckwheat husk is composed mainly of moisture, cellulose, hemicellulose and lignin. As a branched polymer, hemicellulose is usually decomposed at 200~260 ℃ [21]. As a homopolymer, the decomposition temperature of cellulose is 240~350 °C [22]. Lignin usually decomposes at 280~500 ℃ [23]. As shown in Figure 1, the mass loss of buckwheat husk before 110 °C can be attributed mainly to dehydration, which accounts for approximately 7% of the total mass. Between 110~200 ℃, the buckwheat husk remained stable with almost no quality loss. The mass loss of buckwheat husk occurs mainly between 200 and 380 °C, which accounts for approximately 56% and corresponds mostly to the thermal decomposition of cellulose and hemicellulose. At this stage, the mass loss rate of buckwheat husk is very high. After 380 °C, the mass loss is relatively small (approximately 16%) and corresponds mainly to the decomposition of lignin. The weight of the final product was approximately 21% of the weight of the original buckwheat husk. The TG results are similar to the TG results in the literature [24]. The test results show that the weight of buckwheat husk decreases very little after 500 °C. Moreover, an excessively high pyrolysis temperature will lead to the complete decomposition of lignin, resulting in

the collapse of the structure [25]. Therefore, the carbonization temperature of buckwheat husk during the preparation of AC was chosen to be 500 °C.

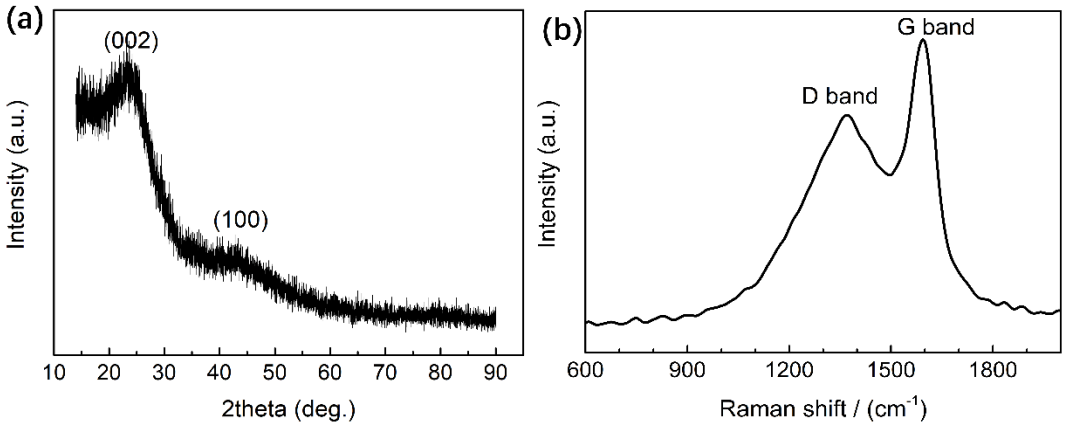

Figure 2. XRD pattern (a) and Raman spectrum (b) of husk-based char (BHC)

Figure 2(a) shows the XRD pattern of BHC. There are broad diffraction peaks at approximately 24° and 43°, which correspond to the (002) and (100) diffraction of graphitic carbon, respectively. However, compared with the diffraction peak of graphitic carbon, which occurs at approximately 25°, the (002) diffraction peak of BHC shifts slightly toward the small diffraction angle direction. At the same time, the broad angle and low intensity characteristics of the (100) peak indicate that the as-prepared BHC is amorphous [26]. Raman spectroscopy is often used to characterize the degree of order and defects in carbon materials. Generally, there are two broad peaks in the Raman spectrum of polycrystalline graphitic carbon, which are the D peak at approximately 1355 cm^{-1} and the G peak at approximately 1580 cm^{-1}. The D and G peaks represent the stretching vibrations of sp3 and sp2 carbon atoms, respectively. In addition, the integrated area ratio of the D peak and G peak (I_D/I_G) can characterize the degree of disorder of the material. The larger the I_D/I_G is, the higher the degree of disorder [27]. The Raman spectrum of BHC is shown in Figure 2 (b). The D and G peaks are located at 1369 cm^{-1} and 1594 cm^{-1}, respectively, with an I_D/I_G of 4.58. The Raman spectrum results indicate that BHC has a high degree of disorder, which is consistent with the XRD results.

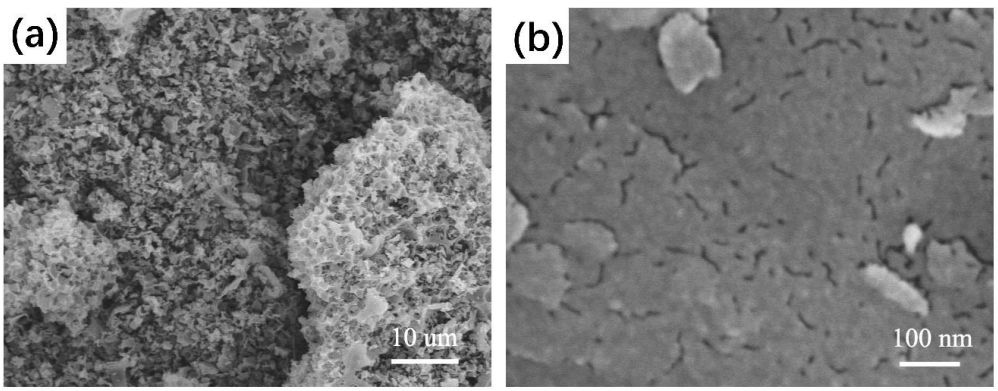

Figure 3. SEM images of BHC at magnifications of 1k (a) and 100k (b)

As shown in Figure 3, at a magnification of 1k, the sample is in the form of an inter-crosslinked granular structure and uniform in size. When the magnification is increased to 100k, a certain number of crack-like pores are visible on the surface of the sample, and the pore distribution is homogeneous. These pores will facilitate the penetration of KOH into the BHC during the subsequent activation process and thereby improve the activation efficiency.

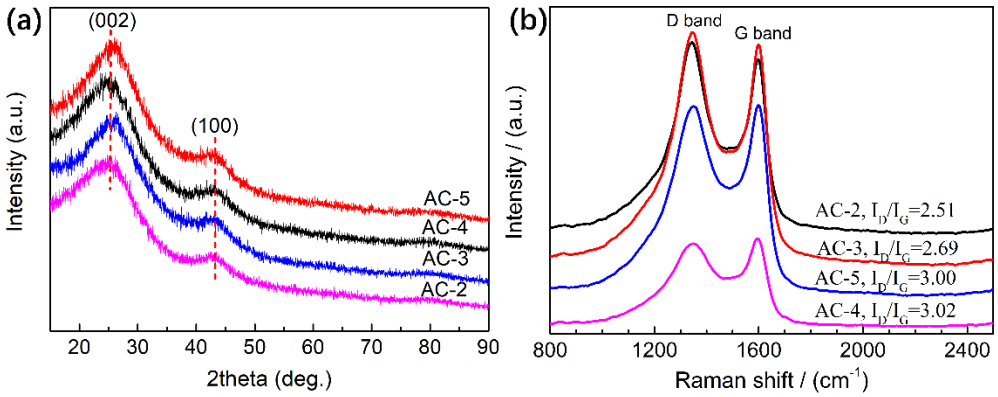

Figure 4. XRD patterns (a) and Raman spectrum (b) of ACs

Figure 4(a) shows the XRD patterns of the AC samples. All samples show broad diffraction peaks at 25° and 43°, corresponding to the (002) and (100) diffraction peaks, respectively, indicating that all AC samples were amorphous. However, compared with BHC, the (002) diffraction peaks shift slightly in the large-angle diffraction direction, and the intensity of the diffraction peaks increases significantly, indicating that the degree of order of the AC samples is higher than the degree of order of BHC, because BHC is a carbonization product at 500 °C, while ACs are activation products at 800 °C. Increasing the temperature can improve the degree of graphitization of the material [28], and a high degree of graphitization is beneficial to improve the conductivity of AC, thereby increasing the power density of the related supercapacitor.

Similar to BHC, all AC samples exhibit Raman peaks at approximately 1360 and 1590 cm^{-1}, corresponding to the D and G peaks, respectively (Figure 4(b)). However, compared with BHC, all AC samples have lower I_D/I_G, indicating that AC samples have a higher degree of order than BHC, consistent with the XRD results. The I_D/I_G values for AC-2, AC-3, AC-4, and AC-5 are 2.51, 2.69, 3.00, and 3.02, respectively, indicating that an increase in the alkali-char ratio will lead to a decrease in the degree of order of the resulted AC. The higher the alkali-char ratio is, the more KOH is used, and therefore, more defects are created.

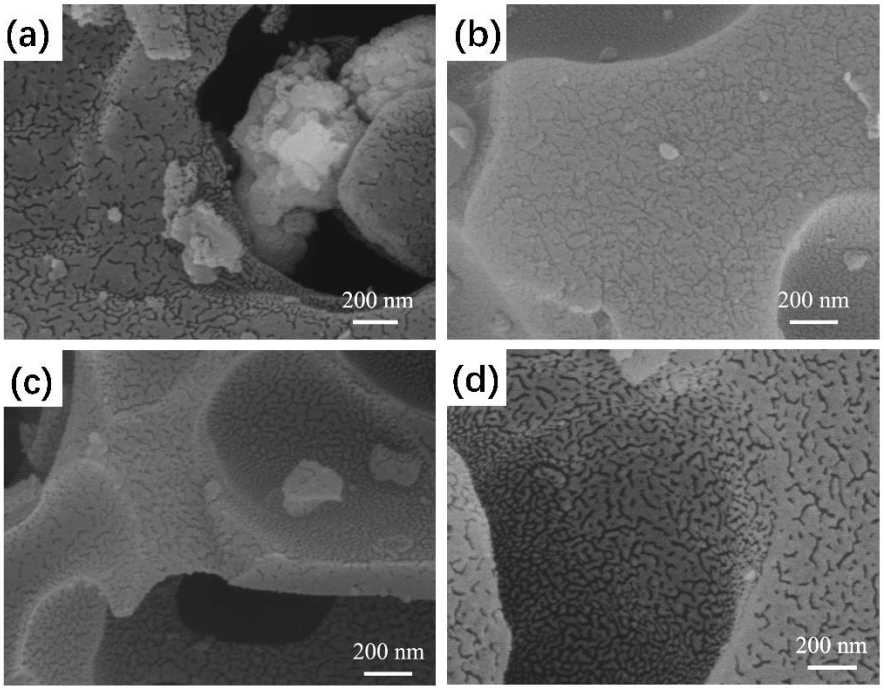

Figure 5. SEM images of AC-2 (a), AC-3 (b), AC-4 (c) and AC-5 (d)

Figure 5 illustrates the SEM images of all AC samples. There are numerous crack-like pores on the surface of all samples. The pore size is very uniform, indicating that BHC was uniformly activated under various alkali-char ratios. In addition, with the increase in the alkali-char ratio, the density of pores on the surface of AC grows gradually, indicating that increasing the amount of KOH can effectively create more pores, thereby increasing the specific surface area and pore volume. Furthermore, compared with AC-4, the pore size of AC-5 is significantly larger, indicating that when the alkali-char ratio reaches a certain value, a further increase in the alkali-char ratio can increase the pore size of the AC.

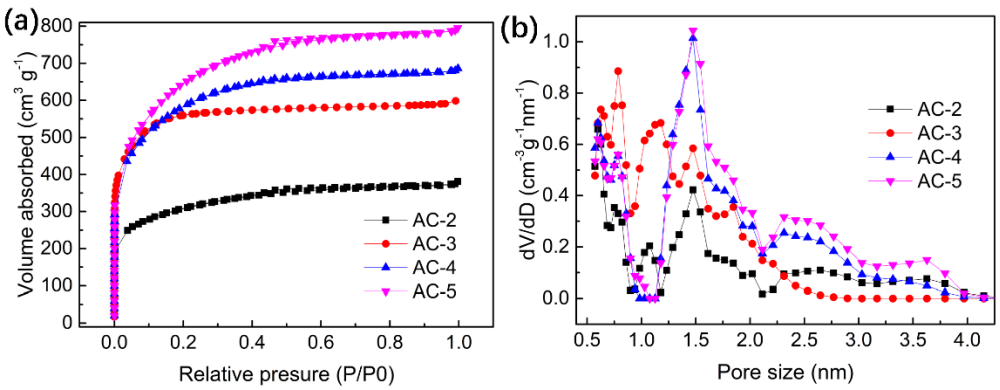

Figure 6. Adsorption and desorption isotherms of ACs (a), pore size distribution of ACs (b)

As shown in Figure 6 (a), the isotherms of all AC samples are a mixture of Type I and Type V. In the low-pressure region (P/P_0<0.5), the amount of N_2 adsorbed increases rapidly, indicating that each

sample has abundant micropores. In the relatively high-pressure region, the amount of N_2 adsorbed continues to increase, indicating that there are a certain number of mesopores in the samples. At the same time, with the increase in the alkali-char ratio, the adsorption capacity increases continuously. When the alkali-char ratio increases from 2 to 3, the adsorption capacity grows the most significantly. Furthermore, there are obvious hysteresis loops in the isotherms of AC-2 and AC-5, indicating that they have more mesopores. As shown in Figure 6 (b), the pores of all samples are mainly micropores and mesopores of narrow width. Compared with micropores, AC-2 has a larger proportion of mesopore pore volume, which is beneficial to obtain a larger average pore diameter. The mesopore volume of AC-3 is very small, and its pores are mainly micropores. The micropore distributions of AC-4 and AC-5 are very similar, but AC-5 has a larger mesopore volume.

Table 1. Porosity parameters of ACs

Samples	S_{BET} ($m^2 g^{-1}$)	R_s [a] (%)	V_{total} ($cm^3 g^{-1}$)	D_{aver} (nm)	C_g ($F g^{-1}$)	C_a [b] ($\mu F cm^{-2}$)
AC-2	1070	77	0.59	2.20	139	13.0
AC-3	2021	95	0.93	1.83	162	8.0
AC-4	2127	86	1.06	1.99	242	11.4
AC-5	2347	78	1.23	2.10	295	12.6

[a] R_s, Ratio of S_{micro} to $S_{BET;}$ [b] C_a, Ratio of C_g to S_{BET}

The porosity parameters of ACs are shown in Table 1. The low alkali-char ratio of AC-2 resulted in insufficient activation and low S_{BET} and V_{total}. However, AC-2 has the largest average pore size and the smallest ratio of S_{micro} to S_{BET}. When the alkali-char ratio is increased from 2 to 3, the S_{BET} and V_{total} grow by 88.9% and 57.6%, respectively. However, the ratio of S_{micro} to S_{BET} increases, and the average pore diameter decreases significantly. With the increase in the alkali-char ratio, the S_{BET}, V_{total} and average pore diameter (D_{aver}) all grow gradually. Among all samples, AC-5 has the largest S_{BET} and V_{total}, and the ratio of S_{micro} to S_{BET} is close to the ratio of S_{micro} to S_{BET} of AC-2.

3.2. Electrochemical properties

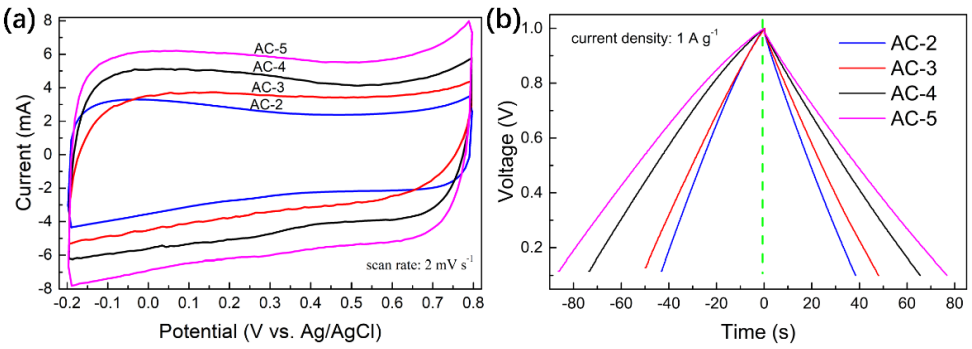

Figure 7. CV (a) and GCD (b) curves of ACs

As shown in Figure 7(a), at a scan rate of 2 mV s^{-1}, the CV curves of various AC samples possess obvious rectangular characteristics in the potential range of -0.2~0.8 V, indicating that the prepared ACs are suitable electrode materials for supercapacitors. However, compared with the standard rectangular curve of the ideal electric double layer electrode, there is an obvious deviation in the CV curve of the actual AC electrodes. The CV curves show that at the moment when the potential scanning direction is suddenly reversed, there is a hysteresis in the response current. A certain period of transition time is required for the response current to achieve a stable value. The value of the transition time is related mainly to the equivalent series resistance (R_s) of the electrode in addition to the electrode capacity. In the case of the same electrode composition and electrolyte, R_s depends mainly on the mass transfer resistance of the electrode, which is closely related to the pore structure of the AC, especially the D_{aver}. The larger the D_{aver} is, the shorter the transition time. Therefore, a large average pore diameter will facilitate the transport of electrolyte ions, thereby reduce the transition time. As seen from Figure 7(a), in the order of transition time from long to short, the AC samples are ranked as AC-3, AC-4, AC-5 and AC-2, consistent with the D_{aver} results shown in Table 1.

Figure 7(b) shows the GCD curves of capacitors based on different ACs with a charge-discharge current density of 1 A g^{-1}. The GCD curves of various AC capacitors have good triangular symmetry, showing the excellent performance of electric double layer capacitors. The C_g values of various ACs are shown in Table 1. With the increase in S_{BET}, C_g rises gradually with AC-5, achieving the largest value of 295 F g^{-1}. However, there is no linear relationship between C_g and S_{BET}. Because in addition to S_{BET}, the PSD is also important for the C_g of the capacitor. Micropores with a pore diameter smaller than the size of electrolyte ions do not contribute to C_g because ions cannot penetrate into these micropores. Pores with diameters slightly larger than that of electrolyte ions make the largest contribution to C_g [29]. Area specific capacitance (C_a) represents the capacitance per square centimeter of surface area of the electrode material can provide. Table 1 shows that the larger the D_{aver} is, the larger the C_a. The theoretical value of C_a has been shown to be approximately 20 μF cm^{-2} [29]. The C_a values of AC-2 and AC-5 reach 65% and 63% of the theoretical value, respectively. Both samples have a high specific surface area utilization rate, indicating that their PSD is reasonable.

Table 2. Comparison of properties of various biomass-based ACs

Materials	S_{BET} (m^2 g^{-1})	Electrolyte	Measure current (A g^{-1})	C_g (F g^{-1})	Ref.
litchi shell	1122	6 M KOH	0.1	220	[30]
waste paper	2341	1 M H_2SO_4	0.5	286	[31]
peanut bran	2565	3 M KOH	0.04	188	[32]
coconut kernel	1200	1 M H_2SO_4	0.25	173	[33]

miscanthus grass	1816	6 M KOH`	0.05	203	[34]
soybean meal	1175	3 M KOH	0.04	330	[35]
coconut shell	1847	6 M KOH	1.0	268	[36]
bamboo shoots	1351	1 M Na_2SO_4	1.0	147	[37]
AC-5	2347	0.5 M Na_2SO_4	1.0	295	This work

Table 2 shows the performance comparison of ACs from different biomass wastes. Both the S_{BET} and the C_g of AC-5 are higher than that of most samples reported in the literature. Most studies on AC-based supercapacitors with aqueous electrolytes use acid or base electrolytes. Because higher conductivity and larger specific capacitance are easier to achieve in these electrolytes. However, acidic and alkaline electrolytes are highly corrosive, especially for the metal casings of the supercapacitor cell. This effect is more prominent in the long-term charging and discharging process. Therefore, a neutral electrolyte was chosen in this work. Compared with AC from waste paper using a 1 M H_2SO_4 electrolyte, AC-5 obtained a similar C_g with a similar S_{BET}, but at a higher current density and in a neutral electrolyte [31]. Likewise, although coconut shell-based AC used a high-concentration alkaline electrolyte (6 M KOH), AC-5 achieved a specific capacitance 27 F/g higher than that of the former at the same current density in 0.5 M Na_2SO_4 [36]. Furthermore, in a Na_2SO_4 electrolyte with a similar concentration and at the same current density, both the S_{BET} and the C_g of AC-5 are approximately twice that of AC derived from bamboo shoots [37]. All these are highly related to the composition and the structure of buckwheat husk and the porosity of the resulted AC.

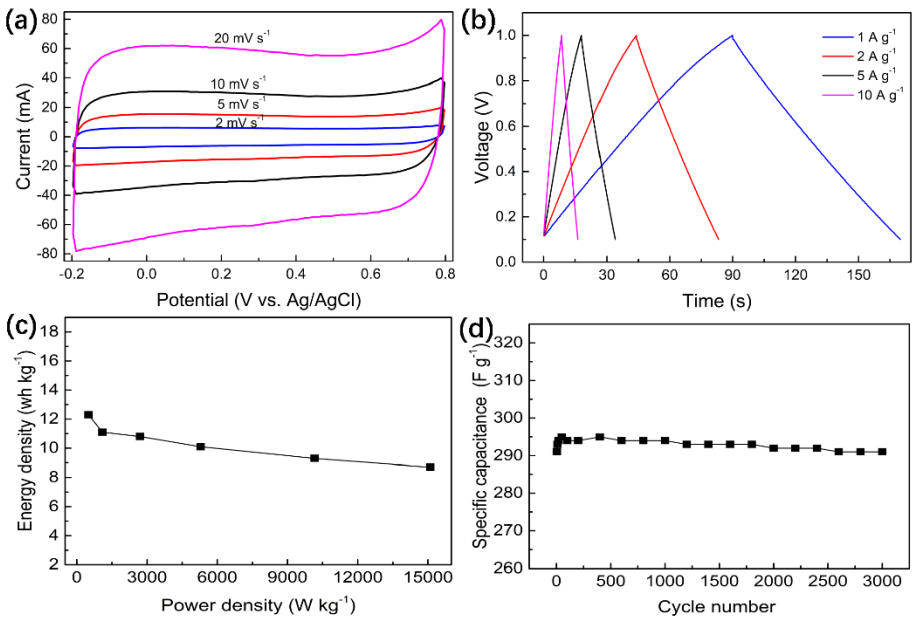

Figure 8. CV (a), GCD (b), Ragone plot (c) and cycling lifetime (d) of the supercapacitor based on AC-5

As shown in Figure 8(a), at different scanning rates, the CV curves of AC-5 maintain excellent rectangular characteristics. Even at a scan rate of 20 mV s^{-1}, the transition time of the response current is short. With the growth of the scanning rate, the response current at each potential increases almost linearly, showing excellent rate characteristics. Similarly, under different current densities, the GCD curves of the supercapacitor based on AC-5 maintain excellent triangular symmetry properties. As the current density increased from 1 A g^{-1} to 10 A g^{-1}, the specific capacitance retention remained at 90.3%. The Ragone plot (Figure 8 (c)) shows that at a power density of 500 W kg^{-1}, an energy density of 12.3 Wh kg^{-1} is achieved. When the power density is increased by a factor of 30, the energy density retention rate is still as high as 70.5%. Cyclic stability is also an important parameter to evaluate the performance of supercapacitors. As shown in Figure 8(d), supercapacitors based on AC-5 maintain excellent capacitance stability throughout the cycle-life test, except for the slight fluctuations in specific capacitance during the first few dozen cycles due to insufficient wetting of the electrodes. After 3000 charge-discharge cycles, the specific capacitance retention rate remains at 98.5%, showing perfect cycle stability.

4. CONCLUSIONS

Activated carbon with a specific surface area up to 2347 m^2 g^{-1} and an average pore diameter of 2.1 nm was prepared from buckwheat husk using KOH as an activator. The micropores of the prepared AC are concentrated mainly in the range of 1~2 nm, and the mesopores in 2 ~ 4 nm. The specific surface area utilization rate reaches 63% of the theoretical value. The as-prepared AC exhibits excellent electric double-layer capacitance properties in both CV and GCD tests. At a current density of 1 A g^{-1}, the specific capacitance of the AC is as high as 295 F g^{-1}. At a power density of 500 W kg^{-1}, the energy density reaches 12.3 Wh kg^{-1}. When the power density is increased by a factor of 30, an energy density retention rate of up to 70.5% is achieved. After 3000 charge-discharge cycles, the specific capacitance retention rate remains at 98.5%. The preparation of AC from buckwheat husks can not only avoid the problems of resource waste and environmental pollution caused by the traditional disposal of buckwheat husk but also produce supercapacitor electrode materials with high added value, providing a new approach for the utilization of biomass waste.

ACKNOWLEDGMENTS
This work is financially supported by the National Natural Science Foundation of China (No. 60901051), Shenzhen Foundation for Science and Technology Development Guided by the Central Government (No. 2021Szvup053) and Science and Technology Foundation of Jiangxi Province Department of Education (No. GJJ170323).

References

1. J. Xiao, J.W. Han, C. Zhang, G.W. Ling, F.Y. Kang, Q.H. Yang, *Adv. Energy Mater*., 12 (2022) 17.
2. A. Das, B. Raj, M. Mohapatra, S.M. Andersen, S. Basu, *Wiley Interdisciplinary Reviews-Energy and Environment*, 11 (2022) 36.

3. M. Ates, A. Chebil, O. Yoruk, C. Dridi, M. Turkyilmaz, *Ionics*, 28 (2022) 27.
4. W.L. Zhang, J. Yin, C.W. Wang, L. Zhao, W.B. Jian, K. Lu, H.B. Lin, X.Q. Qiu, H.N. Alshareef, *Small Methods*, 5 (2021) 24.
5. J.F. Wang, H.P. Yang, Q.Q. Sun, C.S. Zhou, X.Z. Zhang, L.F. Ge, X.R. Ma, *Mater. Lett*., 285 (2021) 4.
6. C.K. Roy, S.S. Shah, A.H. Reaz, S. Sultana, A. Chowdhury, S.H. Firoz, M.H. Zahir, M.A.A. Qasem, M.A. Aziz, *Chem.-Asian J*., 16 (2021) 296.
7. J.H. Yu, X. Li, Z.X. Cui, D. Chen, X.C. Pang, Q. Zhang, F.F. Shao, H.Z. Dong, L.Y. Yu, L.F. Dong, *Renew. Energy*, 163 (2021) 375.
8. J.H. Zhang, H. Chen, J.B. Bai, M. Xu, C.L. Luo, L.X. Yang, L.J. Bai, D.L. Wei, W.X. Wang, H.W. Yang, *J. Alloy. Compd*., 854 (2021) 10.
9. C. Xu, Z.Y. Hu, X. Wang, C.Y. Wang, D.J. Huang, Y. Qian, *Int. J. Electrochem. Sci*., 16 (2021) 9.
10. L.H. Zheng, M.H. Chen, S.X. Liang, Q.F. Lu, *Diam. Relat. Mat*., 113 (2021) 10.
11. M.G. Shang, J. Zhang, X.C. Liu, Y. Liu, S.P. Guo, S.M. Yu, S. Filatov, X.B. Yi, *Appl. Surf. Sci*., 542 (2021) 11.
12. B.G. Liu, R. Shi, R.F. Chen, C.H. Wang, K. Zhou, Y.D. Ren, Z. Zeng, Y.Y. Liu, L.Q. Li, *Appl. Surf. Sci.,* 538 (2021) 9.
13. R. Hossain, R.K. Nekouei, I. Mansuri, V. Sahajwalla, *J. Energy Storage*, 33 (2021) 10.
14. G.F. Zheng, Z.C. Huang, Z. Liu, *J. Power Sources*, 482 (2021) 13.
15. D.F. Guo, Z.J. Li, P. Liu, M. Sun, *Int. J. Hydrog. Energy*, 46 (2021) 8197.
16. J. Pena, A. Villot, C. Gerente, *Biomass and Bioenergy*, 132 (2020).
17. S.V. Gnedenkov, D.P. Opra, L.A. Zemnukhova, S.L. Sinebryukhov, I.A. Kedrinskii, O.V. Patrusheva, V.I. Sergienko, *J. Energy Chem*., 24 (2015) 346.
18. M. Chen, X. Kang, T. Wumaier, J. Dou, B. Gao, Y. Han, G. Xu, Z. Liu, L. Zhang, *Journal of Solid State Electrochemistry*, 17 (2012) 1005.
19. S.J. Song, F.W. Ma, G. Wu, D. Ma, W.D. Geng, J.F. Wan, *J. Mater. Chem*. A, 3 (2015) 18154.
20. L.J. Xie, G.H. Sun, F.Y. Su, X.Q. Guo, Q.Q. Kong, X.M. Li, X.H. Huang, L. Wan, W. Song, K.X. Li, C.X. Lv, C.M. Chen, *J. Mater. Chem*. A, 4 (2016) 1637.
21. F.M. Gírio, C. Fonseca, F. Carvalheiro, L.C. Duarte, S. Marques, R. Bogel-Łukasik, *Bioresour. Technol.*, 101 (2010) 4775.
22. R. Rinaldi, F. Schüth, *ChemSusChem*, 2 (2009) 1096.
23. J. Zakzeski, P.C.A. Bruijnincx, A.L. Jongerius, B.M. Weckhuysen, *Chem. Rev*., 110 (2010) 3552.
24. K. Yu, Z. Zhang, J. Liang, C. Liang, *Diam. Relat. Mat*., 119 (2021).
25. M. Molina-Sabio, F. Rodríguez-Reinoso, *Colloids and Surfaces A: Physicochemical and Engineering Aspects,* 241 (2004) 15.
26. G. Moreno-Fernández, J.L. Gómez-Urbano, M. Enterría, T. Rojo, D. Carriazo, *J. Mater. Chem*. A, 7 (2019) 14646.
27. A. Adan-Mas, L. Alcaraz, P. Arevalo-Cid, F.A. Lopez-Gomez, F. Montemor, *Waste Manage*., 120 (2021) 280.
28. P. Li, C.N. Feng, H.P. Li, X.L. Zhang, X.C. Zheng, *J. Alloy. Compd*., 851 (2021) 10.
29. J. Chmiola, G. Yushin, Y. Gogosti, C. Portet, P. Simon, P. Taberna, *Science*, 313 (2006) 1760.
30. N. Zhao, P. Zhang, D. Luo, W. Xiao, L. Deng, F. Qiao, *J. Alloy. Compd*., 788 (2019) 677.
31. D. Puthusseri, V. Aravindan, B. Anothumakkool, S. kurungot, S. Madhavi, S. Ogale, *Small*, (2014) 4395.
32. W.W. Kang, B.P. Lin, G.X. Huang, C.X. Zhang, Y.H. Yao, W.T. Hou, B. Xu, B.L. Xing, *J. Mater. Sci.-Mater. Electron.*, 29 (2018) 6361.
33. B. Kishore, D. Shanmughasundaram, T.R. Penki, N. Munichandraiah, *J. Appl. Electrochem*., 44 (2014) 903.
34. G.A. Yakaboylu, C.L. Jiang, T. Yumak, J.W. Zondlo, J.X. Wang, E.M. Sabolsky, *Renew. Energy*, 163 (2021) 276.

35. H. Zhao, B. Xing, C. Zhang, G. Huang, Q. Liu, G. Yi, J. Jia, M. Ma, Z. Chen, C. Zhang, *J. Alloy. Compd.,* 766 (2018) 705.
36. L. Sun, C. Tian, M. Li, X. Meng, L. Wang, R. Wang, J. Yin, H. Fu, *J. Mater. Chem*. A, 21 (2013) 6462.
37. J.J. Han, Q. Li, J.Q. Wang, J.L. Ye, G.S. Fu, L. Zhai, Y.W. Zhu, *J. Mater. Sci.-Mater. Electron*., 29 (2018) 20991.

© 2022 The Authors. Published by ESG (www.electrochemsci.org). This article is an open access article distributed under the terms and conditions of the Creative Commons Attribution license (http://creativecommons.org/licenses/by/4.0/).